New Gravity Wave Treatments for GISS Climate Models

MARVIN A. GELLER,* TIEHAN ZHOU,+ RETO RUEDY,# IGOR ALEINOV,+ LARISSA NAZARENKO,+ NIKOLAI L. TAUSNEV,# SHAN SUN,@,& MAXWELL KELLEY,+ AND YE CHENG+

* *Stony Brook University, School of Marine and Atmospheric Sciences, Stony Brook, New York*
+ *NASA Goddard Institute for Space Studies, and Center for Climate Systems Research, Columbia University, New York, New York*
# *NASA Goddard Institute for Space Studies, and SGT, Inc., New York, New York*
@ *NASA Goddard Institute for Space Studies, New York, New York, and Massachusetts Institute of Technology, Cambridge, Massachusetts*

(Manuscript received 18 August 2010, in final form 26 January 2011)

ABSTRACT

Previous versions of GISS climate models have either used formulations of Rayleigh drag to represent unresolved gravity wave interactions with the model-resolved flow or have included a rather complicated treatment of unresolved gravity waves that, while being climate interactive, involved the specification of a relatively large number of parameters that were not well constrained by observations and also was computationally very expensive. Here, the authors introduce a relatively simple and computationally efficient specification of unresolved orographic and nonorographic gravity waves and their interaction with the resolved flow. Comparisons of the GISS model winds and temperatures with no gravity wave parameterization; with only orographic gravity wave parameterization; and with both orographic and nonorographic gravity wave parameterizations are shown to illustrate how the zonal mean winds and temperatures converge toward observations. The authors also show that the specifications of orographic and nonorographic gravity waves must be different in the Northern and Southern Hemispheres. Then results are presented where the nonorographic gravity wave sources are specified to represent sources from convection in the intertropical convergence zone and spontaneous emission from jet imbalances. Finally, a strategy to include these effects in a climate-dependent manner is suggested.

1. Introduction

The Goddard Institute for Space Studies (GISS) Model-E climate model has been described in Schmidt et al. (2006), and this was the GISS model that generated results that were used in Solomon et al. (2007), the most recent Intergovernmental Panel on Climate Change assessment. There were three versions of GISS Model-E that were described in Schmidt et al. (2006). Two of these, M20 and F20, had model tops at 0.1 hPa and 20 layers in the vertical, with M20 having 4°(latitude) × 5° (longitude) horizontal resolution and F20 having 2° × 2.5° horizontal resolution. The other, M23, had 4° × 5° horizontal resolution and 23 layers, with a top at 0.002 hPa. The Arakawa B grid was used in all of these models, and a sigma vertical coordinate was used up to 150 hPa with a pressure vertical coordinate above. The basic model physics for these models was described in Schmidt et al. (2006) and previous GISS publications referenced therein. Schmidt et al. (2006) described how the results from these models compared to a variety of diagnostics from observations.

Although most of the model physics used in these models were pretty much state-of-the-art, the treatments of unresolved gravity waves were not. Both M20 and F20 models used a Rayleigh drag scheme at the model top together with another simple Rayleigh drag scheme in the model interiors, above 150 hPa. While these parameterizations were meant to crudely represent the influence of unresolved gravity waves, their treatments were not self consistent in this regard. The M23 model used a climate-dependent gravity wave drag owing to Rind et al. (1988). This included treatments of orographic drag and

& Current affiliation: Global Systems Division, NOAA Earth System Research Laboratory, Boulder, Colorado.

Corresponding author address: M. A. Geller, Stony Brook University, School of Marine and Atmospheric Sciences, Stony Brook, NY 11794-5000.
E-mail: marvin.geller@sunysb.edu

DOI: 10.1175/2011JCLI4013.1

penetrating convection, shear, and deformation gravity wave sources. While this latter gravity wave treatment adjusts to different climate regimes, it is expensive in terms of computer time and contains a large number of adjustable coefficients that have little in the way of observational constraints.

GISS is now participating in the IPCC Assessment Report 5 (AR5). This has motivated a lot of updating of the various physics packages, and we have been implementing a new gravity wave treatment in the new GISS climate model. In the following, we will describe this, as well as show some comparisons with observations, and discuss how these new gravity wave treatments improve upon the Rayleigh drag parameterization previously used in GISS Model-E.

2. Gravity wave effects

Since the pioneering work of Leovy (1964) and the subsequent papers of Schoeberl and Strobel (1978) and Holton and Wehrbein (1980), the importance of parameterizing the effects of unresolved gravity waves to successfully model the middle atmosphere circulation has been appreciated. Later, Palmer et al. (1986) and McFarlane (1987) showed that the effects of unresolved, orographically forced gravity waves should be parameterized to obtain good simulations of the troposphere. Even with the inclusion of orographic gravity wave parameterizations, however, it is still necessary to parameterize the effects of gravity waves arising from nonorographic sources such as convection, frontogenesis, and jet sources so as to obtain realistic middle atmosphere climatologies in climate models with reasonable resolution. There exist high-resolution atmospheric general circulation models that give quite realistic atmospheric structure without any treatment of unresolved gravity waves (e.g., Watanabe et al. 2008), but these models are too expensive to run with extensive climate interactions (e.g., ocean, cryosphere, biosphere) using the present generation of computers. Thus, climate models will require parameterizations of unresolved gravity waves for at least the next decade or so.

The development of gravity wave parameterizations began with the classical work of Lindzen (1981), and this was followed by several different formulations for parameterizing nonorographic gravity waves (e.g., Hines 1997; Alexander and Dunkerton 1999; Warner and McIntyre 2001). There have been more recent formulations for orographic gravity wave parameterizations (e.g., Lott and Miller 1997; Scinocca and McFarlane 2000), and there have also been recent efforts toward including physically based, nonorographic gravity wave treatments (i.e., that use the modeled phenomena in the climate model for sources of gravity waves in their parameterization) in papers such as those by Charron and Manzini (2002) and Richter et al. (2010).

Our efforts have been motivated by the following considerations. We want

1) methods for gravity wave parameterization that give realistic atmospheric structures, interannual variability, responses to climate perturbations, and realistic transport characteristics;
2) parameterizations that are physically well-founded;
3) parameterizations that are computationally efficient; and
4) parameterizations that can be adapted to respond to a changing climate.

The previously used J drag in GISS Model-E (Schmidt et al. 2006) does not satisfy the above criteria in that, although it is meant to simulate gravity wave effects, it behaves quite differently physically. The J-drag in Model-E responds to local winds rather than to wind filtering by levels below. Also, the J-drag provides a relaxation toward a motionless state for both the zonally averaged wind and for zonally asymmetric wind. The climate responses to models with Rayleigh drag have been investigated by Shepherd et al. (1996), as well as by Shepherd and Shaw (2004), and they found that models with Rayleigh drag gave spurious climate responses. The desirability of momentum conservation for gravity wave parameterization was investigated in a series of papers by Shepherd and Shaw (2004), Shaw and Shepherd (2007), and Shaw et al. (2009). While it is true that Model-E did seek to conserve momentum by balancing the momentum deposition above with a counterbalancing momentum deposition below, the manner in which this is done is rather arbitrary and does not physically correspond to the workings of gravity waves.

Our initial efforts use the orographic gravity wave parameterization of McFarlane (1987) and the nonorographic scheme of Alexander and Dunkerton (1999). These choices were motivated by the following considerations. While the Lott and Miller (1997) and Scinocca and McFarlane (2000) schemes are more realistic than that of McFarlane (1987) in that they include such effects as low-level wave breaking, upstream blocking, and lee-vortex dynamics, they are also more complicated to code for use in the GISS models, whereas the McFarlane scheme involves only simple coding. Furthermore, while some improvements have been noted when these newer schemes are used, these improvements are relatively modest compared with the improvements that are realized when our gravity wave parameterizations are used (e.g., Scinocca et al. 2008) instead of the earlier Rayleigh drag treatments in GISS Model-E.

Our use of the Alexander and Dunkerton (1999) gravity wave scheme was motivated by results in McLandress and Scinocca (2005). They showed that differences in nonorographic gravity wave parameterization schemes were less important than were the proper specifications of the nature of gravity wave sources (e.g., the gravity wave source spectrum). This, together with the fact that the Alexander and Dunkerton gravity wave parameterization allows for particularly simple mapping of the nature of the source spectrum to their effects on the mean flow, motivated our choice for the nonorographic parameterization.

3. Some simple intermediate results

There are several parameters that need to be specified even for our relatively simple choice of schemes. The McFarlane scheme uses variances of elevation calculated from a high-resolution topography dataset, but one must specify values for two parameters. One of these is the critical Froude number Fr_c, which determines the threshold for gravity wave breaking, and hence the vertical distribution of the gravity wave momentum deposition.[1] We have taken Fr_c^2 to be 0.5, a conventional value. The other, in McFarlane's notation, is

$$E\frac{\mu_e}{2}h_e^2,$$

where μ_e is a characteristic horizontal wavenumber, h_e is a characteristic wave amplitude, and E is a constant that is meant to represent the wave intermittency. For the results shown in this paper, we have taken $E\mu_e/2$ to be equal to 5.5×10^{-6} m^{-1}, and h_e^2 is taken from the topography height variances in each gridbox.

In the Alexander and Dunkerton scheme, we must specify the shape of the gravity wave spectrum, and this includes specification of a functional form as well as a spectrum-width parameter. We are using the B_2 spectral shape of Gong et al. (2008) with the width parameter c_w equal to 10 m s^{-1} and the source amplitude $B_m = 0.01$ m^2 s^{-2} everywhere in this paper. We use four azimuthal directions (north, east, south, and west) in which the gravity waves are launched. Finally, we launch our nonorographic waves at 100 hPa. This choice is motivated by two considerations. One is that jet imbalances are known to be a source of gravity waves (see J. Gong and M. A. Geller 2011, unpublished manuscript, for example), and the other is that deep convective towers impinging on the tropopause are also known to be a significant wave source, particularly in the tropics.

[1] For consistency and clarity, we use the terminology of Fr as in McFarlane (1987), which is actually the inverse Froude number (Scinocca and McFarlane 2000).

In practice, there is a great deal of "tuning" that goes into the choice of gravity wave parameterization parameters since, until recently, there have been few observations to guide their choice, although this situation is now changing (see Alexander et al. 2010) with the growing literature on observations of gravity waves by various techniques. Both resolved waves and unresolved gravity waves influence the atmospheric zonal-mean wind and temperature states. Given that there are several adjustable parameters in both the McFarlane (1987) orographic gravity wave scheme and in the Alexander and Dunkerton (1999) gravity wave scheme, our philosophy in choosing values for these parameters is to first "tune" the orographic scheme to get the troposphere/lower stratosphere to agree reasonably with Northern Hemisphere winter zonal-mean temperature and wind observations and then to tune the Alexander and Dunkerton (1999) nonorographic gravity wave scheme to agree with wind and temperature observations in the upper stratosphere.

Our discussion in this section is based on a succession of four figures, each comparing the 40-yr European Centre for Medium-Range Weather Forecasts Re-Analysis (ERA-40) with GISS model results that include no specification of gravity wave drag (referred to as GISS-ND); GISS model results with the effects of orographic gravity waves only included (referred to as GISS-OG); and finally GISS model results including both orographic and nonorographic gravity wave effects (GISS-OG&NOG). These simulations have been carried out in an Atmospheric Model Intercomparison Project (AMIP) sense. We have run the model starting in 1979 for 21 years and compare our model climatology for the years 1980–99 with that from ERA-40 for those same years. The horizontal resolution for all the GISS model results shown here is $2° \times 2.5°$ as in GISS Model-E F20 in Schmidt et al. (2006), and the model tops are at 0.1 hPa with 40 layers in the vertical. In these figures, the momentum flux B_t at the 100-hPa source level was specified as 0.0015 kg m^{-1} s^{-2} for both the east–west and north–south azimuth pairs. Sea surface temperatures, ice conditions, ozone, and greenhouse gas concentrations are specified for the modeled years.

Figure 1 shows results for January zonal-mean zonal winds, Fig. 2 results for January zonally averaged temperatures, Fig. 3 for July zonal-mean zonal winds, and Fig. 4 for July zonally averaged temperatures. Looking at Fig. 1, note that the GISS-ND January subtropical jets in both hemispheres compare well with the ERA-40 results in both speed and latitude and the easterly summer jet also looks somewhat reasonable, although there is no evidence in ERA-40 of the double jet structure seen in GISS-ND above ~5 hPa. The GISS-ND winter westerly jet is much too strong, however, with

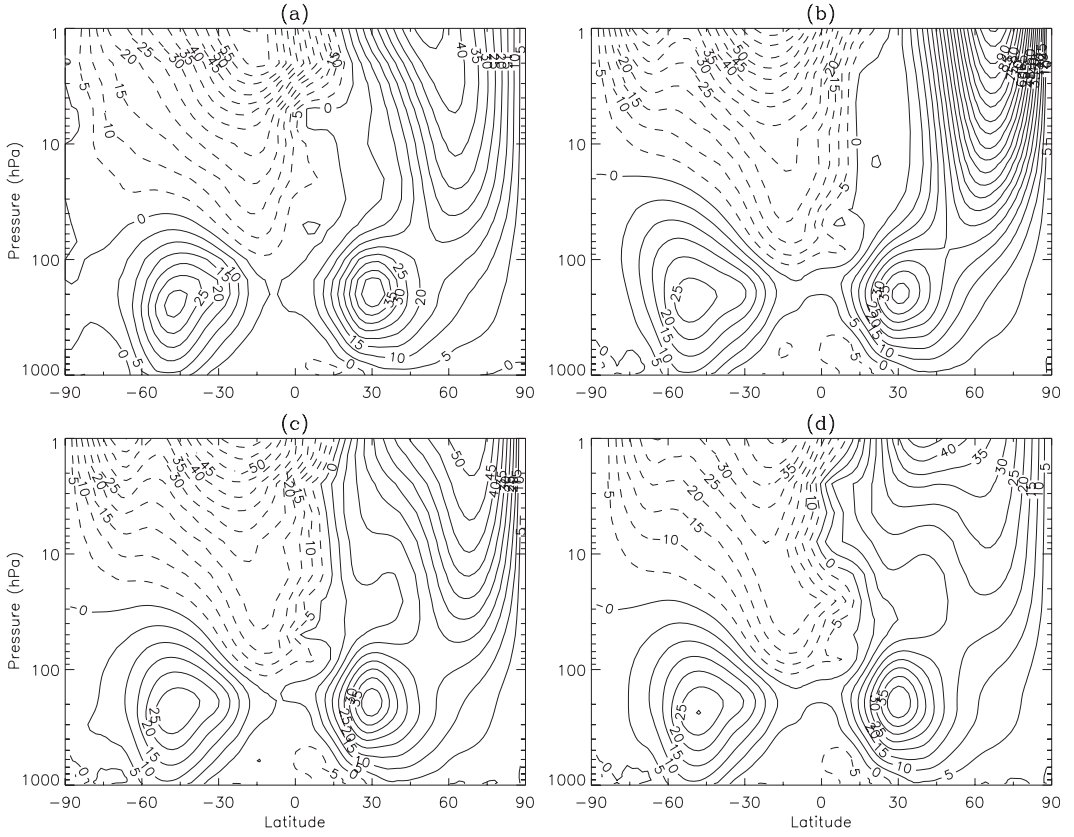

FIG. 1. January zonal mean zonal wind from (a) ERA-40, (b) GISS-ND, (c) GISS-OG, and (d) GISS-OG&NOG. Wind intervals are 5 m s^{-1}. Solid (dashed) lines denote westerly (easterly) winds.

zonal-mean zonal winds of ~100 m s^{-1} at 1 hPa, while ERA-40 only has winds of ~45 m s^{-1}. Note also that the region of relatively weak westerlies between the winter upper and lower jet structures is always above 25 m s^{-1} in GISS-ND while the ERA-40 winds are less than 20 m s^{-1} in this region. The inclusion of orographic drag improves the agreement between our modeled January zonal mean winds and observations. The maximum westerly winds at 1 hPa in GISS-OG are now ~50 m s^{-1}, which is only a bit greater than the ERA-40 winds in this region. Note also that the 30 m s^{-1} contour is at about 25 hPa, 65°N and agrees well with ERA-40, whereas in GISS-ND the 30 m s^{-1} contour was at ~50 hPa, 60°N, so the inclusion of orographic gravity wave drag has reduced the shear in the region between the jets to agree well with observations. With the nonorographic drag included, the maximum westerly winds at 1 hPa are ~ 45 m s^{-1}, located at about 40°N. This is a bit equatorward of what is seen in ERA-40. In GISS-OG&NOG, the minimum winds between the tropopause and polar night jets are less than 20 m s^{-1}, again in agreement with ERA-40. Looking at January summer, however, we see that the maximum easterly winds at 1 hPa are ~45 m s^{-1}, which is less than the ERA-40 observed 65 m s^{-1}, but their latitude agrees well with observations.

In Fig. 2, consistent with the thermal wind relation, the January winter lower-stratosphere temperatures are too cold in GISS-ND, being below −90°C compared to observed values below −70°C. This winter cold bias extends upward through the stratosphere reaching about 50°C at 1 hPa, and there is also a summer warm bias in the GISS-ND of ~10°C at 5 hPa so that the 1-hPa pole-to-pole temperature gradient is ~85°C in GISS-ND and only ~40°C in ERA-40. Consistent with the thermal wind relation, the inclusion of orographic drag has raised the minimum January winter polar night temperatures from −90°C in GISS-ND to about −80°C, which is closer to the ERA-40 polar night temperatures of −70°C. It also has lowered the pressure altitude of the winter polar temperature minimum from ~20 hPa in GISS-ND case to ~40 hPa in GISS-OG, which is closer to the observations (~50 hPa), and the winter cold biases are everywhere less than 15°C. In the January winter hemisphere, the minimum polar night temperatures in GISS-OG&NOG are about −70°C, which are close to those in ERA-40, and their pressure altitudes compare

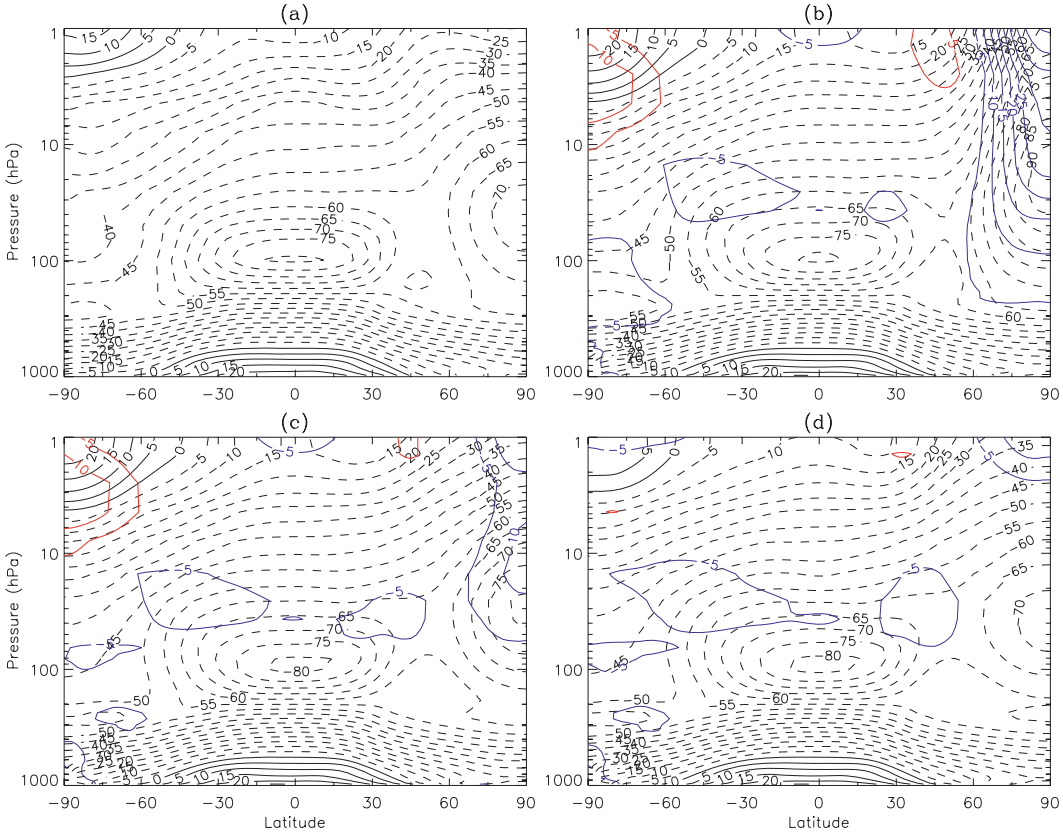

FIG. 2. January zonal mean temperatures (in °C) from (a) ERA-40, (b) GISS-ND, (c) GISS-OG, and (d) GISS-OG&NOG). Solid (dashed) contours indicate temperatures above (below) 0°C. Red (Blue) contours indicate warm (cold) biases from ERA-40, where contour intervals are 5°C.

well. In fact, small cold biases less than 10°C are only seen at midlatitudes in both hemispheres. At 1 hPa, the pole-to-pole temperature gradient is ~40°C, which compares well with ERA-40.

Looking at Fig. 3, the July GISS-ND subtropical jet latitudes and wind speeds compare well with ERA-40. At higher altitudes, both summer and winter wind speeds are too high in GISS-ND, with the maximum modeled winter westerlies being ~175 m s^{-1} at 1 hPa compared to ~95 m s^{-1} maximum ERA-40 wind speeds at 1 hPa. The summer easterlies in GISS-ND are ~65 m s^{-1} at 1 hPa whereas the ERA-40 winds there are ~40 m s^{-1}. The July winter westerlies in GISS-OG are decreased a bit. The maximum westerly winds at 1 hPa in GISS-ND are ~175 m s^{-1} at about 65°S. In GISS-OG, the maximum July westerlies at 1 hPa are ~150 m s^{-1} and are approximately at 60°S. This is compared to westerlies of ~95 m s^{-1} at 1 hPa in ERA-40 that are at about 45°S. Also, note that the minimum winds between the tropopause jet and polar night jet in both GISS-ND and GISS-OG are in excess of 30 m s^{-1}, whereas in ERA-40 they are less than 30 m s^{-1}. The GISS-OG&NOG July maximum winter westerlies are ~135 m s^{-1}, which is about 40 m s^{-1} more than in ERA-40. Also, these maximum westerly winds are at ~60°S, compared to about 50°S in ERA-40. The observed equatorward tilt of the polar night jet seen in ERA-40 is not evident in the GISS-OG&NOG results shown in Fig. 3. The minimum winds between the tropopause jet and polar night jet are above 30 m s^{-1} in GISS-OG&NOG, which is more than in ERA-40. Looking at the July summer easterlies in GISS-OG&NOG, we see that the maximum winds are 55 m s^{-1} located at about 15°N. This is to be compared to the ERA-40 value of ~40 m s^{-1}, which is located at about 30°N.

Figure 4 shows the temperature comparisons for July. The coldest winter lower-stratospheric temperatures in GISS-ND are about −115°C whereas the corresponding ERA-40 temperatures are about −90°C, and the pole-to-pole temperature gradient at 1 hPa in GISS-ND is more than 130°C, whereas the corresponding ERA-40 temperature gradient is again ~40°C. A winter pole cold bias of about −80°C is seen at 1 hPa, with smaller cold biases extending throughout the winter polar stratosphere. A smaller warm bias is seen in the summer upper

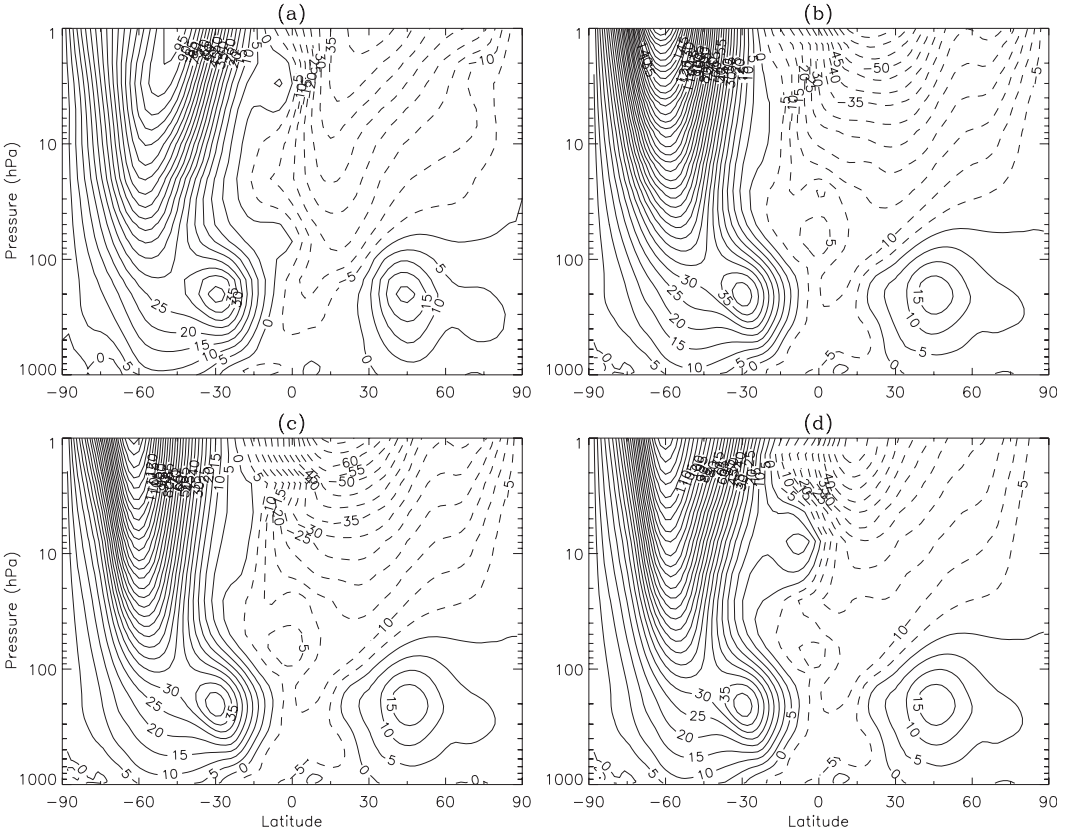

FIG. 3. As in Fig. 1 but for July.

stratosphere. The inclusion of orographic gravity wave effects in GISS-OG has greatly improved the lower-stratosphere polar night temperatures, with minimum stratospheric temperatures of about −95°C centered at about 20 hPa in GISS-OG. The ERA-40 minimum temperatures are about −90°C at about 30 hPa. The GISS-OG winter pole cold biases are about halved relative to those in GISS-ND, and the summer pole warm biases are unchanged. The minimum July stratospheric polar night temperatures in GISS-OG&NOG are about −95°C at about 20 hPa. This is a little higher and colder than in ERA-40, but the winter polar cold biases are little changed from GISS-OG. The warm biases at the summer pole are diminished, with a small summer pole warm bias now seen near 1 hPa. The pole-to-pole temperature gradient at 1 hPa in GISS-OG&NOG is ~70°C, which is about 30°C more than in ERA-40, and is consistent with the stronger winds than in ERA-40.

Summarizing the results shown so far then, it is apparent that the inclusion of orographic gravity wave effects has brought both the January and July zonal-mean zonal winds and temperatures into much closer agreement with observations, particularly in the lower stratosphere, but still having substantial disagreement with observations. Including both orographic and nonorographic gravity wave effects, the zonal-mean zonal winds and zonally averaged temperatures are closer to the ERA-40 climatology, but the degree of agreement between model results and ERA-40 is quite different in the Northern and Southern Hemispheres. We will consider this point more in the next section.

4. Nonuniformity of nonorographic gravity wave sources

While the inclusion of orographic and nonorographic gravity wave treatments have brought the GISS model results closer to ERA-40 climatology results, several problems remain. Perhaps the most notable is seen in Fig. 4, where the GISS-OG&NOG July pole-to-pole temperature gradient at 1 hPa is ~70°C, whereas in ERA-40 it is only ~40°C. This is manifested in the July zonal-mean zonal winds being too strong in GISS-OG&NOG in both hemispheres. Interestingly, the January GISS-OG&NOG pole-to-pole temperature gradient is actually consistent with ERA-40 (35°C compared to 40°C), and this is consistent with weaker zonal-mean zonal winds in the January GISS-OG&NOG Southern Hemisphere than are seen

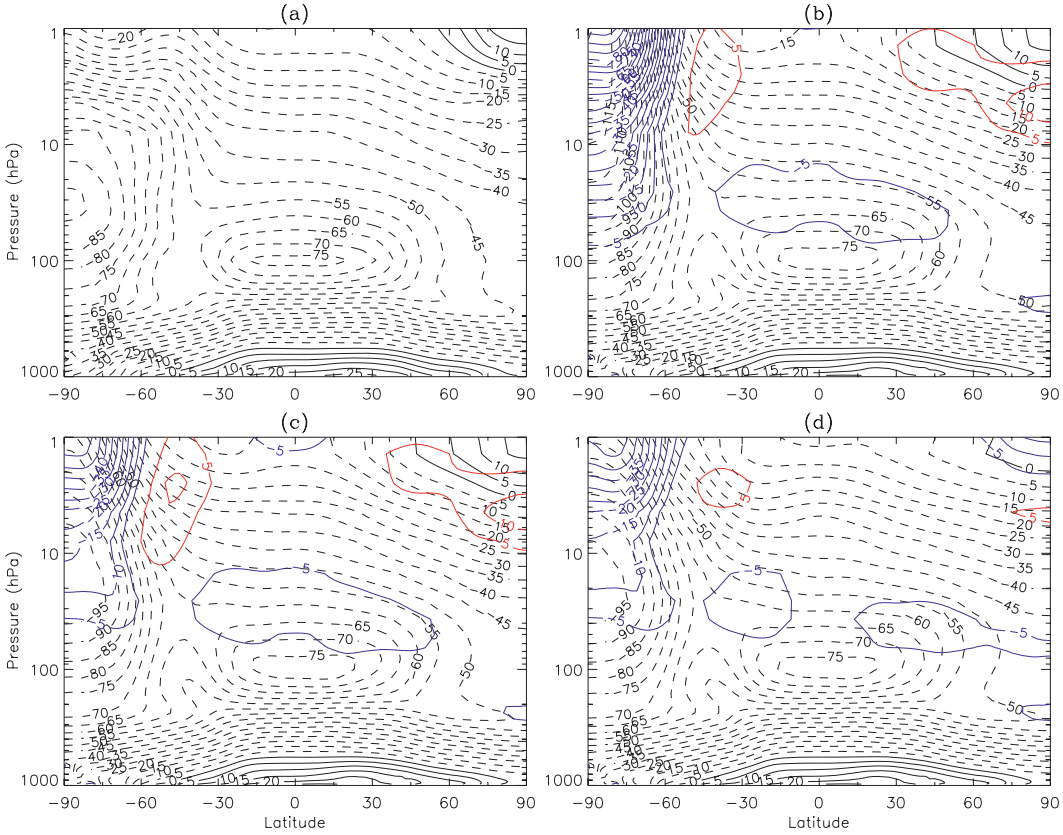

FIG. 4. As in Fig. 2 but for July.

in ERA-40. This suggests that a globally and temporally uniform nonorographic gravity wave scheme is not appropriate, a fact previously noted by Charron and Manzini (2002), Garcia et al. (2007), and Richter et al. (2010).

Since the GISS-OG&NOG January pole-to-pole temperature gradient results agree well with ERA-40 in January, we have experimented with what globally uniform nonorographic gravity wave source function is needed to bring the July temperature gradient into agreement with observations. Figure 5 shows GISS-OG&NOG January and July zonal-mean zonal wind and temperature distributions for $B_t = 0.004$ kg m^{-1} s^{-2}. Note first that the July pole-to-pole temperature gradient at 1 hPa is about 50°–55°C, somewhat larger than the July ERA-40 value; however for this value of B_t, the January temperature gradient at 1 hPa is only ~25°C, which is about 15°C less than observed. Interestingly, there is a January summer polar cold bias at all altitudes and a July cold bias over both poles in this case. Consistent with these temperature distributions, the July Southern Hemisphere polar night jet is slightly stronger than in ERA-40, but the summer Northern Hemisphere easterlies are much too weak in Fig. 5. Interestingly though, there is evidence of equatorial westerly to easterly shear regions for this large value of B_t that was not so evident in Figs. 1 and 3. Examining the equatorial winds, we see that this is produced by a QBO-like wind oscillation but with an annual period (see the appendix for more information). The GISS-OG&NOG January zonal-mean zonal winds in Fig. 5 are too weak in the winter lower stratosphere but are of reasonable magnitude in the upper stratosphere, albeit located at too low latitudes. The January summer easterlies are much too weak for this large value of B_t. The winter westerlies show no equatorward tilt, such as seen in ERA-40, in Fig. 5 in either January or July.

Clearly then, some nonuniformity in nonorographic gravity wave source functions is required to bring GISS-OG&NOG results into agreement with observations, but there should be physical justification for this nonuniformity. Remembering that some of the physical sources for nonorographic gravity waves are convection, fronts, and spontaneous emission from jets, one can get an idea of what the nature of their temporal and spatial distribution might be. In a recent paper by Richter et al. (2010), they included explicitly computed gravity wave source functions in the Whole Atmosphere Community Climate Model (WACCM). Their physical sources for

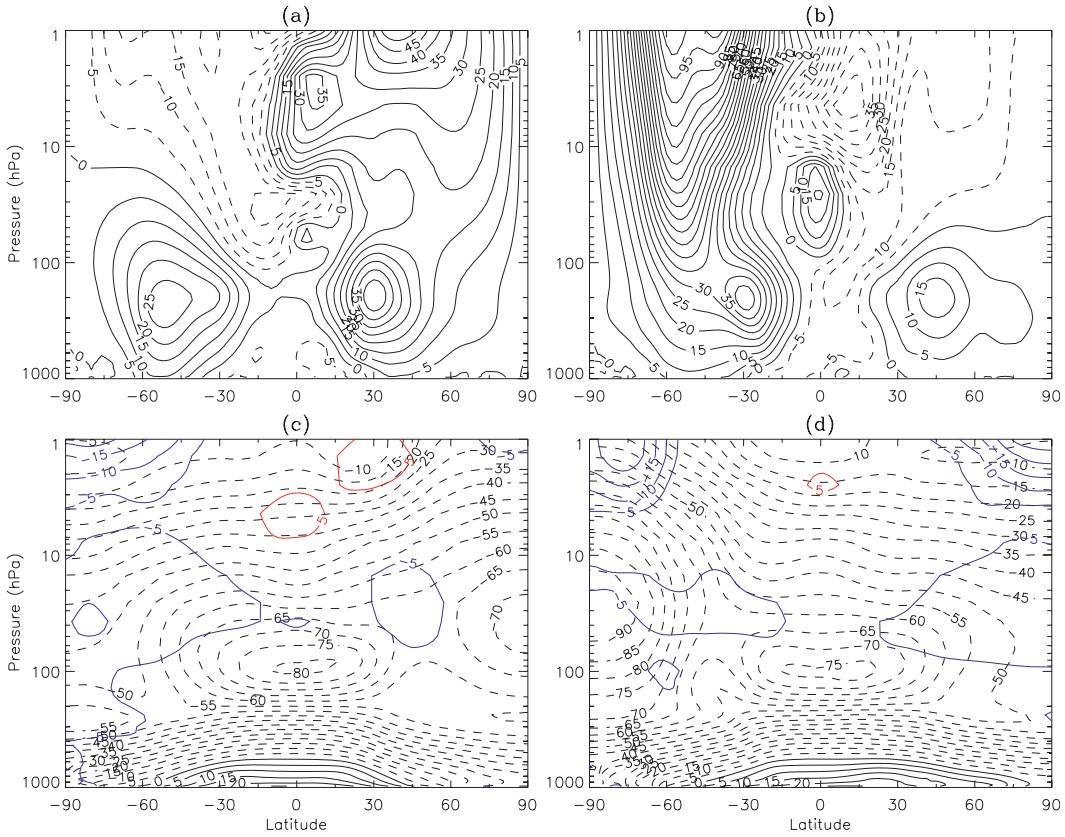

FIG. 5. Zonal-mean zonal winds for (a) January and (b) July from GISS-OG&NOG with $B_t = 0.004$ kg m^{-1} s^{-2}. The corresponding zonally averaged temperatures are shown for (c) January and (d) July.

nonorographic gravity waves were convection and emission from frontal systems. Their resulting momentum fluxes at 100 hPa are shown in their Figs. 2 and 3.

Conceptually then, we will only consider two types of physical sources for nonorographic gravity waves—convection and spontaneous emission from jets. This is different from Richter et al. (2010) in that their nonorographic gravity wave sources are convection and emission from fronts. Richter et al. (2010) indicate that their frontal source for gravity waves should often be collocated with jet sources, but there are two important differences. One is that the jet source should be at higher altitudes than the frontal sources, and the other is that jet sources should be more ubiquitous than frontal sources. J. Gong and M. A. Geller (2011, unpublished manuscript) have performed a study in which they trace back gravity waves that they observe using high vertical resolution radiosonde data. They find that in the cases they consider, they can use ray tracing to establish that the source of these gravity waves is associated with jet imbalances. Furthermore, they use the linear model of Wang and Zhang (2010) to show that these source jet imbalance regions give rise to gravity waves having frequencies and wavenumbers that are consistent with the radiosonde observations.

For these reasons, we consider the nonorographic gravity wave sources to be at a pressure altitude of 100 hPa (Richter et al. 2010 have their nonorographic gravity wave source altitude at 600 hPa) and to have the spatial and temporal dependence that we expect from jet imbalance and convection sources. We consider both of these gravity wave source functions to have the same spectral shape [the B_2 function of Gong et al. (2008) with $c_w = 10$ m s^{-1}), and tune the magnitudes of their momentum fluxes B_t to give zonal-mean zonal winds and zonally averaged temperatures that are consistent with ERA-40. The wind and temperature results are shown in Fig. 6. Figure 7 shows the temporal and spatial distribution of B_t that were used in GISS-OG&NOG to obtain these results. This nonorographic gravity wave source function at 100 hPa was specified to have a Gaussian shape in latitude for both the tropical convective source and extratropical jet imbalance source, and these Gaussians were centered at latitudes that were meant to represent the seasonal variation of the intertropical convergence zone and the polar jet streams. The relatively broad width

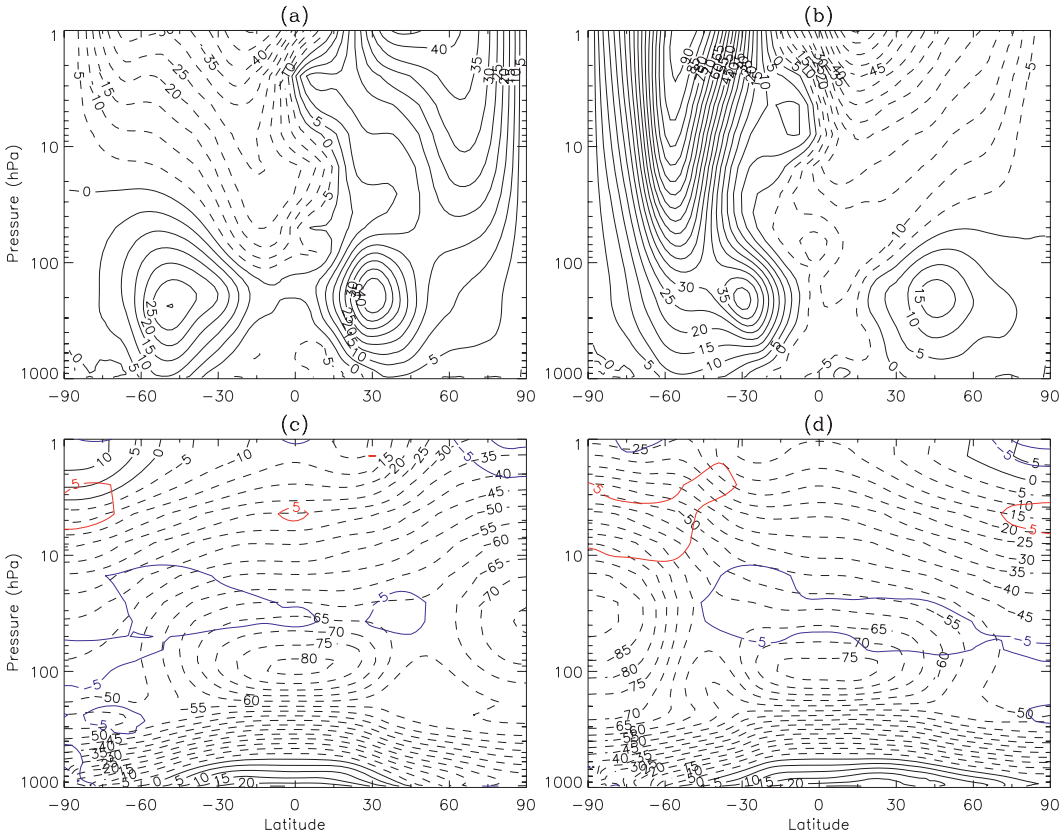

FIG. 6. Zonal-mean zonal winds and temperatures in (a),(c) January and (b),(d) July for GISS-OG&NOG with values explained in the text and shown in Fig. 7.

of the extratropical Gaussians are meant to represent the splitting and meandering of these jets. A background nonorographic gravity wave source with $B_t = 0.001$ kg m^{-1} s^{-2} is taken to exist everywhere and is superposed upon our idealizations of the tropical convective and jet stream sources. The background source is meant to represent any number of nonorographic gravity wave sources that are not associated with ITCZ convection and jet imbalance. This overall picture is consistent with the gravity wave climatologies derived from satellite, radiosondes, and GPS data (e.g., Alexander and Barnet 2007; Wang and Geller 2003; Tsuda et al. 2000) that show greater gravity wave activity in the stratosphere during winter than summer. Note the time-varying gravity wave source function shown in Fig. 7 is larger in the Southern Hemisphere than in the Northern Hemisphere. Their ratio is reasonable given the stronger Southern Hemisphere storm tracks found by Guo et al. (2009) and the fact that the jet imbalance gravity wave source involves the square of the jet strength (see Wang and Zhang 2010, for example).

Both the GISS-OG&NOG January zonally averaged temperatures and zonal-mean zonal winds in Fig. 6 agree well with ERA-40 in the Northern and Southern Hemispheres in terms of the jet stream strengths and locations, the region of minimum shear between the tropopause jet and the polar night jet (although these July winds are still about 5 m s^{-1} too strong), and the equatorward tilt of the

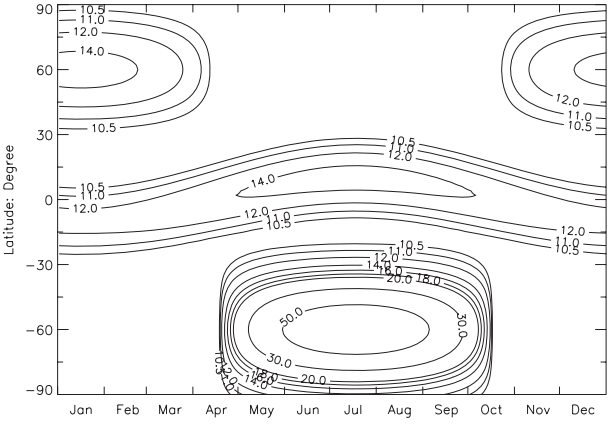

FIG. 7. Spatial and temporal distribution of B_t used for the spatially and temporally varying nonorographic gravity wave source function in GISS-OG&NOG to generate the results in Fig. 6.

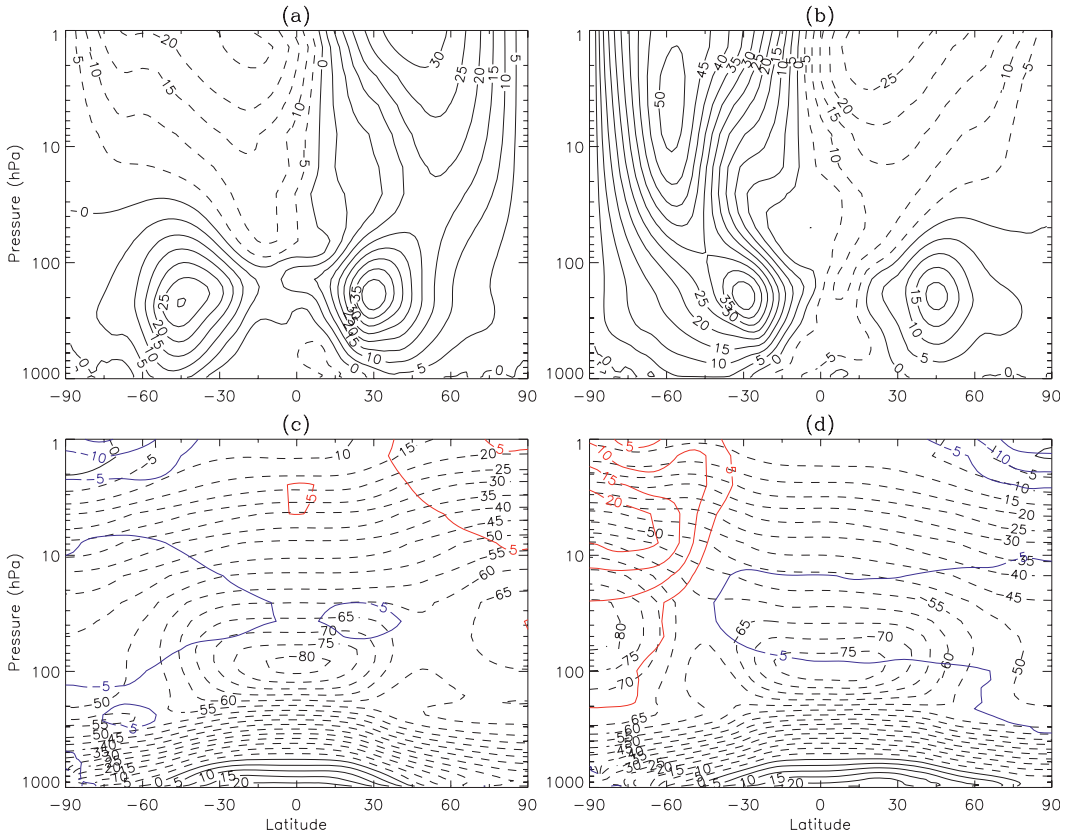

FIG. 8. As in Fig. 6 but using the J-drag in Schmidt et al. (2006).

polar night jet. In July, the wind systems agree almost as well as in January. The polar night jet shows the proper equatorward slope, and the region of minimum shear between the lower- and upper-jet systems in the Southern Hemisphere agrees reasonably with ERA-40. Consistent with the thermal wind relationship, the temperatures also show good agreement with ERA-40. In January, the lower-stratosphere minimum is a little colder than in ERA-40 and is located at the same altitude. The January pole-to-pole temperature gradient is ~45°C in the GISS-OG&NOG model compared to 40°C in ERA-40, and the stratopause temperature distributions are very similar. In July, the modeled minimum winter lower-stratospheric temperatures compare well with ERA-40 and they occur at the same altitude as in ERA-40. The temperature differences from ERA-40 only exceed 5°C in a few places, such as in a belt of small cold biases centered at about 50 hPa and is rather narrow in its altitude extent, which extends from low latitudes to the winter pole. Small cold biases near 1 hPa give modeled pole-to-pole temperature gradients that are about 5°C too high in January and agree well in July with those in ERA-40.

To further emphasize the need for a nonuniform orographic gravity wave source, we have calculated the global- and temporal-average value of the source function shown in Fig. 7 to be 0.001 32 kg m^{-1} s^{-2}, which is just a little less than the value of 0.0015 kg m^{-1} s^{-2}, used to generate Figs. 1–4. Thus, it is not that the globally averaged value of the nonorographic gravity wave source that gives the good results shown in Fig. 6 but rather the spatial and temporal distribution of these nonorographic gravity wave sources.

Schmidt et al. (2006) show the comparison between their M20, M23, and F20 GISS Model-E modeled zonal-mean zonal winds with the COSPAR International Reference Atmosphere (CIRA) results in their Fig. 16. To examine the changes that result from including both orographic and nonorographic gravity waves compared to the J-drag used in Schmidt et al. (2006), we have preformed an identical AMIP-style run using the J-drag formulation of Schmidt et al. These results are shown in Fig. 8. Looking first at the zonal-mean zonal winds, both summer and winter stratospheric winds are much too weak in January and July. Consistent with this, the modeled January and July pole-to-pole temperature gradients at 1 hPa are much too weak compared to observations. A similar pattern of relatively small cold biases in the summer polar stratosphere are seen in both January and July with warm

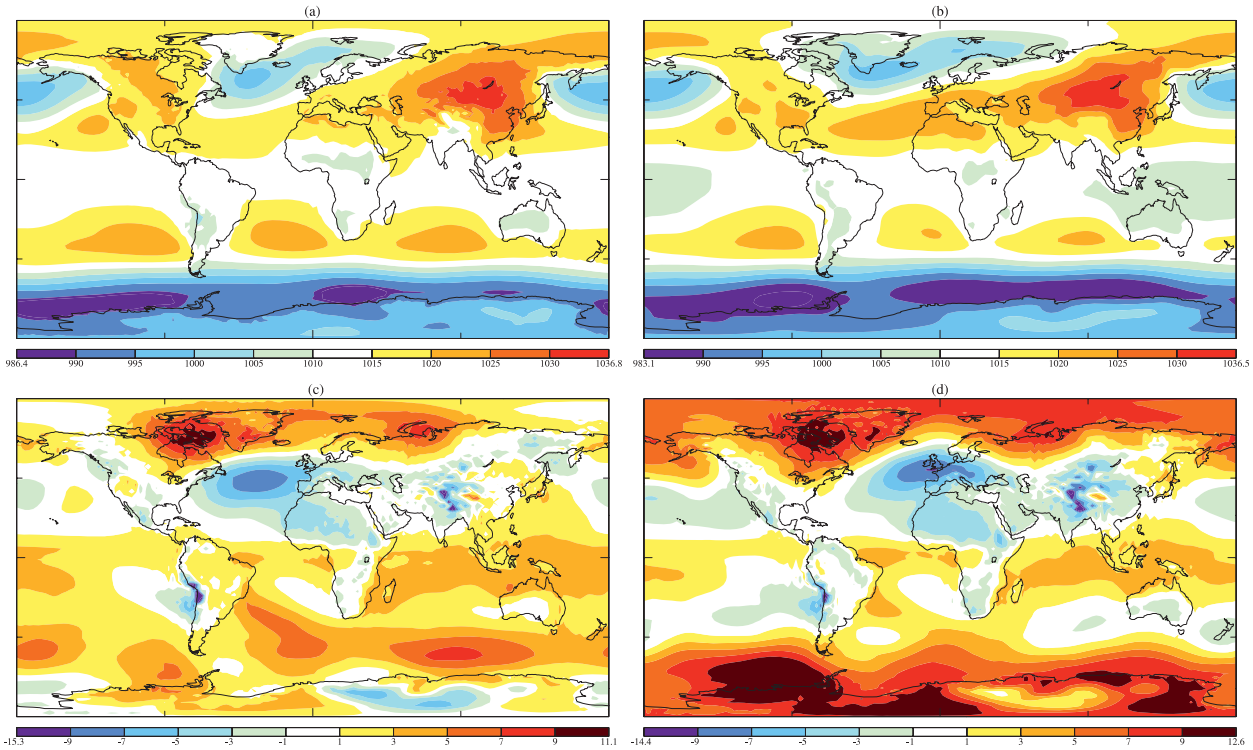

FIG. 9. January sea level pressure (hPa) distribution from (a) GISS-OG&NOG for 1980–99; (b) ERA-40 for 1980–1999; (c) their difference; and (d) the difference from ERA-40 when J-drag is used.

biases in the summer polar stratosphere that are relatively small in January but exceed 20°C in July. This is likely due to excessive dissipation owing to the imposed J-drag that gives rise to an excessive summer-to-winter meridional circulation with its accompanying excessive winter downwelling and summer upwelling.

It should be noted that comparing results obtained using J-drag values, which were tuned for the GISS Model-E in Schmidt et al. (2006), in the newer model for which our gravity wave treatment was tuned is not a completely fair comparison. However, it should also be noted that the J-drag results shown here have very similar deficiencies to those of the M20 and F20 results shown in Schmidt et al., so we think that we are identifying improvements mainly due to using our gravity wave treatments instead of the J-drag to represent gravity wave effects.

Noting that all gravity wave tuning has been focused on obtaining reasonable troposphere/stratosphere zonal-mean zonal wind and temperature structures, while using approaches that are defensible in terms of atmospheric physics, we now look at some sea level pressure (SLP) results to see how they compare with the earlier results of Schmidt et al. (2006). In doing so, it should be noted that there have been other improvements in the physical treatments in the GISS model, so one cannot attribute improvements in model results as being strictly due to our gravity wave treatments. On the other hand, there is a clear indication that by obtaining the troposphere/stratosphere zonal-mean zonal wind and temperature structure, we have also improved the troposphere–surface simulation.

Figure 9 shows our model 1980–99 January SLP climatology in comparison with the 1980–99 ERA-40 climatology, as well as a similar comparison using the Model-E J-drag, described in Schmidt et al. (2006). Note that Fig. 9c shows maximum positive sea level differences between our model and ERA-40 of less than ~7.0 hPa everywhere except for over Greenland, the Arctic in the Northern Hemisphere, and a small region north of Antarctica at about 100°E. We do see a sizable negative SLP difference (~10 hPa) in the North Atlantic and in smaller regions where there is very high topography such as in the Himalayas and Andes. The J-drag differences shown in Fig. 9d, on the other hand, while being comparable at midlatitudes are much worse at high latitudes. This is likely due to too much polar downwelling induced by the excessive dissipation. Figure 10 shows a similar comparison for July. Looking at the July SLP, we see that GISS-OG&NOG has SLP too large by up to ~12 hPa over Greenland and north of Antarctica at about 0°. Large negative differences (up to ~15 hPa) from ERA-40 are

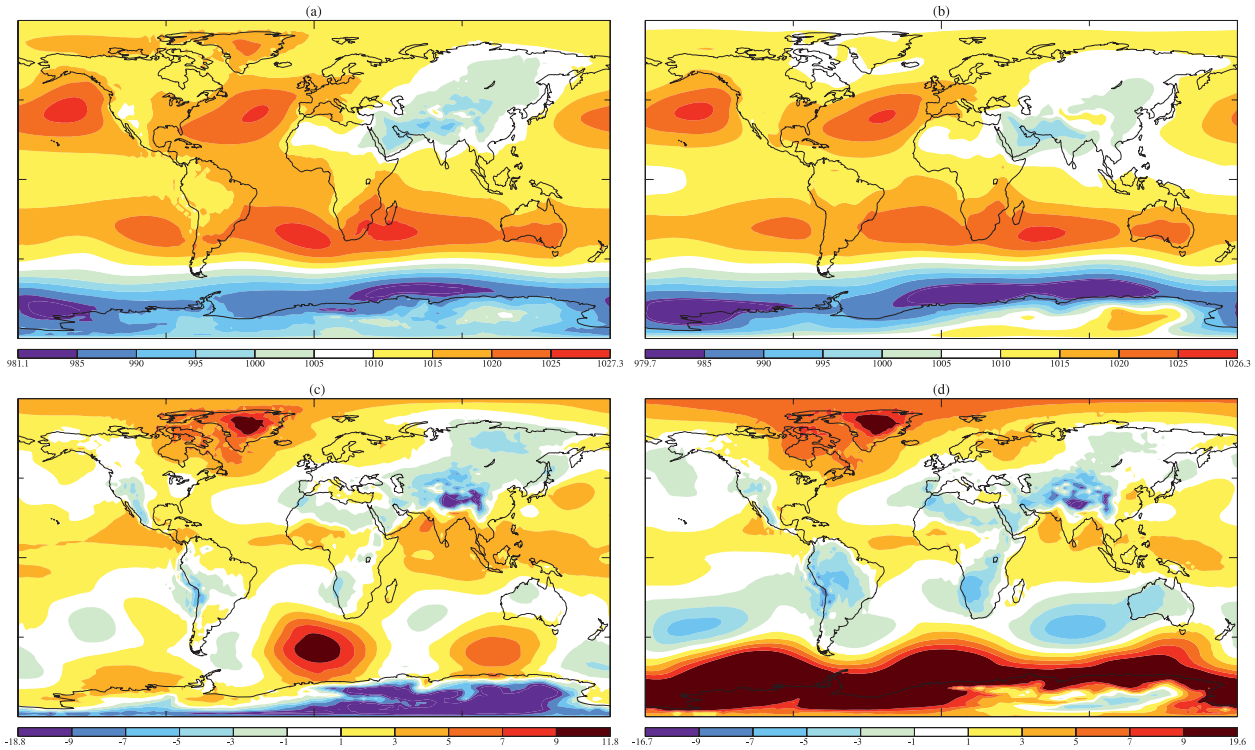

FIG. 10. As in Fig. 9 but for July.

confined to high-topography regions over the Himalayas and Antarctica, with smaller departures over the Rockies and Andes regions. Quantitative comparisons of SLP in these regions of high topography are questionable, however, since they depend on methods for hypsometric correction. The J-drag SLP differences from ERA-40 in July are generally larger, again particularly at high latitudes.

5. Toward climate interactive gravity wave sources

The agreement between the GISS-OG&NOG model results and ERA-40 is very encouraging. These results were obtained with climatological specifications of the gravity wave sources, but suggest a strategy to make these specifications interactive with a changing climate. This is to make the jet stream spontaneous emission sources dependent on the model-generated jet stream strengths and locations. There are various alternatives for this. One could calculate nonlinear imbalance terms (e.g., Medvedev and Gavrilov 1995; Plougonven and Zhang 2007) and launch gravity waves from these regions. One could use the Wang and Zhang (2010) methodology to determine the strength of the emitted gravity waves and use the results to construct jet-dependent gravity wave momentum fluxes. One could also use the Beres et al. (2005) results to make an interactive parameterization for the convectively generated gravity waves in the same way as was done in Richter et al. (2010).

6. Concluding comments

In this paper, we have only compared modeled zonal-mean zonal winds, zonally averaged temperatures, and surface pressure distributions. We are now in the process of performing more extensive diagnostics on our model results, which is underway and is showing promising results. This will be the subject of a companion paper.

We want to stress that our formulation for the parameterization of unresolved gravity waves has not been tuned for good simulations of parameters like sea level pressure or to obtain good stratospheric transports. Rather, we have implemented our parameterizations in a physically reasonable manner and have tuned these to get reasonable simulations of troposphere–stratosphere zonal-mean zonal wind and temperature climatologies. We have taken this approach since these are the parameters that are directly impacted by these parameterizations. It is very encouraging that this approach gives good results for sea level pressure and constituent transports (as will be shown in a future paper).

There are more improvements to be implemented. For instance, we will be implementing a more state-of-the-art treatment of orographic gravity waves, and this

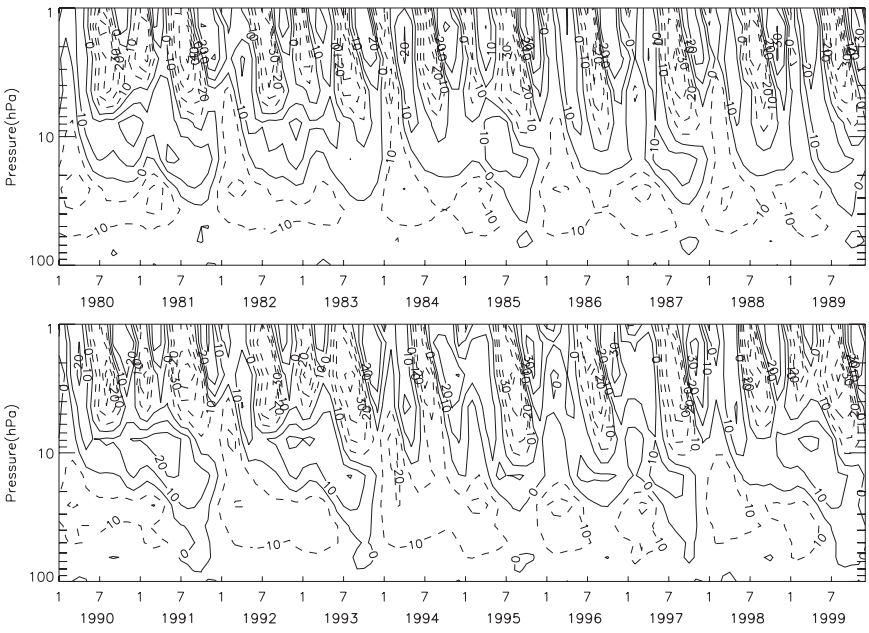

FIG. A1. Time series of stratospheric monthly mean winds over the equator from GISS-OG&NOG using a globally uniform value of $B_t = 0.002$ kg m^{-1} s^{-2}.

may lead to some changes in the parameter settings for the nonorographic gravity waves. We will also implement climate-dependent gravity wave source functions. Finally, we will be investigating the influence of our model top since this is known to affect the structure of the resolved waves and their effects on the mean flow.

Acknowledgments. Financial support for this work came from NASA's Modeling and Analysis and Atmospheric Composition, Modeling, and Analysis programs. The authors also thank Dr. John Scinocca and an anonymous reviewer for their helpful comments, which led to an improved paper.

APPENDIX

Equatorial Oscillation in the Model

In seeking to better understand the QBO-like equatorial shears, seen in Fig. 5, we examined time series of the modeled stratospheric equatorial winds for various values of a globally uniform value of B_t at 100 hPa. We found that for B_t values of 0.0005 and 0.001 kg m^{-1} s^{-2}, a semiannual oscillation was seen above 10 hPa (not shown); however, when $B_t = 0.002$ and 0.0025 kg m^{-1} s^{-2}, a clear quasi-biennial oscillation was seen in the lower stratosphere (see Fig. A1, for example). For $B_t = 0.003$–0.0045 kg m^{-1} s^{-2}, the oscillation was found to have an annual period (not shown).

When we compared the equatorial wind oscillation with globally uniform $B_t = 0.0015$ kg m^{-1} s^{-2} with that obtained with the B_t values shown in Fig. 7, the equatorial wind oscillations were very similar. This motivates us toward future research where we increase our equatorial momentum fluxes in the tropics from the values shown in Fig. 7 to see whether we will be able to get a self-consistent QBO, together with mean extratropical winds and temperatures, and interannual variability in the model that is consistent with observations.

REFERENCES

Alexander, M. J., and T. J. Dunkerton, 1999: A spectral parameterization of mean-flow forcing due to breaking gravity waves. *J. Atmos. Sci.,* **56,** 4167–4182.

——, and C. Barnet, 2007: Using satellite observations to constrain parameterizations of gravity wave effects for global models. *J. Atmos. Sci.,* **64,** 1652–1665.

——, and Coauthors, 2010: Recent developments in gravity wave effects in climate models and the global distribution of gravity wave momentum flux from observations and models. *Quart. J. Roy. Meteor. Soc.,* **136,** 1103–1124.

Beres, J. H., R. R. Garcia, B. A. Boville, and F. Sassi, 2005: Implementation of a gravity wave source spectrum parameterization dependent on the properties of convection in the Whole Atmosphere Community Climate Model (WACCM). *J. Geophys. Res.,* **110,** D10108, doi:10.1029/2004JD005504.

Charron, M., and E. Manzini, 2002: Gravity waves from fronts: parameterization and middle atmosphere response in a general circulation model. *J. Atmos. Sci.,* **59,** 923–941.

Garcia, R. R., D. R. Marsh, D. E. Kinnison, B. A. Boville, and F. Sassi, 2007: Simulation of secular trends in the middle

atmosphere, 1950–2003. *J. Geophys. Res.,* **112,** D09301, doi:10.1029/2006JD007485.

Gong, J., M. A. Geller, and L. Wang, 2008: Source spectra information derived from U.S. high-resolution radiosonde data. *J. Geophys. Res.,* **113,** D10106, doi:10.1029/2007JD009252.

Guo, Y., E. K. M. Chang, and S. S. Leroy, 2009: How strong are the Southern Hemisphere storm tracks? *Geophys. Res. Lett.,* **36,** L22806, doi:10.1029/2009GL040733.

Hines, C. O., 1997: Doppler-spread parameterization of gravity-wave momentum deposition in the middle atmosphere. Part 1: Basic formulation. *J. Atmos. Sol. Terr. Phys.,* **59,** 371–386.

Holton, J. R., and W. M. Wehrbein, 1980: A numerical model of the zonal mean circulation of the middle atmosphere. *Pure Appl. Geophys.,* **118,** 284–306.

Leovy, C. B., 1964: Simple models of thermally driven mesospheric circulation. *J. Atmos. Sci.,* **21,** 327–341.

Lindzen, R. S., 1981: Turbulence and stress owing to gravity wave and tidal breakdown. *J. Geophys. Res.,* **86,** 9707–9714.

Lott, F., and M. J. Miller, 1997: A new subgrid-scale orographic gravity wave parameterization: Its formulation and testing. *Quart. J. Roy. Meteor. Soc.,* **123,** 101–127.

McFarlane, N. A., 1987: The effect of orographically excited gravity wave drag on the general circulation of the lower stratosphere and troposphere. *J. Atmos. Sci.,* **44,** 1775–1800.

McLandress, C., and J. F. Scinocca, 2005: The GCM response to current parameterizations of non-orographic gravity wave drag. *J. Atmos. Sci.,* **62,** 2394–2413.

Medvedev, A. S., and N. M. Gavrilov, 1995: The nonlinear mechanism of gravity wave generation by meteorological motions in the atmosphere. *J. Atmos. Terr. Phys.,* **57,** 1221–1231.

Palmer, T. N., G. J. Shutts, and R. Swinbank, 1986: Alleviation of a systematic westerly bias in general circulation and numerical weather prediction models through an orographic gravity wave drag parameterization. *Quart. J. Roy. Meteor. Soc.,* **112,** 1001–1031.

Plougonven, R., and F. Zhang, 2007: On the forcing of inertia–gravity waves by synoptic scale flows. *J. Atmos. Sci.,* **64,** 1737–1742.

Richter, J. H., F. Sassi, and R. R. Garcia, 2010: Toward a physically based gravity wave source parameterization in a general circulation model. *J. Atmos. Sci.,* **67,** 136–156.

Rind, D., R. Suozzo, N. K. Balachandran, A. Lacis, and G. Russell, 1988: The GISS global climate–middle atmosphere model. Part I: Model structure and climatology. *J. Atmos. Sci.,* **45,** 329–370.

Schmidt, G. A., and Coauthors, 2006: Present-day atmospheric simulations using GISS Model E: Comparison to in situ, satellite, and reanalysis data. *J. Climate,* **19,** 153–192.

Schoeberl, M. R., and D. F. Strobel, 1978: The zonally averaged circulation of the middle atmosphere. *J. Atmos. Sci.,* **35,** 577–591.

Scinocca, J. F., and N. A. McFarlane, 2000: The parameterization of drag induced by stratified flow over anisotropic orography. *Quart. J. Roy. Meteor. Soc.,* **126,** 2353–2393.

——, ——, M. Lazare, J. Li, and D. Plummer, 2008: Technical note: The CCCma third generation AGCM and its extension into the middle atmosphere. *Atmos. Chem. Phys.,* **8,** 7055–7074.

Shaw, T. A., and T. G. Shepherd, 2007: Angular momentum conservation and gravity wave drag parameterization: implications for climate models. *J. Atmos. Sci.,* **64,** 190–203.

——, M. Sigmond, and T. G. Shepherd, 2009: Sensitivity of simulated climate to conservation of momentum in gravity wave parameterization. *J. Climate,* **22,** 2726–2742.

Shepherd, T. G., and T. A. Shaw, 2004: The angular momentum constraint on climate sensitivity and downward influence in the middle atmosphere. *J. Atmos. Sci.,* **61,** 2899–2908.

——, K. Semeniuk, and J. N. Koshyk, 1996: Sponge layer feedbacks in middle-atmosphere models. *J. Geophys. Res.,* **101,** 23 447–23 464.

Solomon, S., D. Qin, M. Manning, M. Marquis, K. Averyt, M. M. B. Tignor, H. L. Miller Jr., and Z. Chen, Eds., 2007: *Climate Change 2007: The Physical Science Basis*. Cambridge University Press, 996 pp.

Tsuda, T., M. Nishida, C. Rocken, and R. H. Ware, 2000: A global morphology of gravity wave activity in the stratosphere revealed by the GPS occultation data (GPS/MET). *J. Geophys. Res.,* **105,** 7257–7727.

Wang, L., and M. A. Geller, 2003: Morphology of gravity wave energy as observed from four years (1998–2001) of high resolution U.S. radiosonde data. *J. Geophys. Res.,* **108,** 4489, doi:10.1029/2002JD002786.

Wang, S., and F. Zhang, 2010: Sources of gravity waves within a vortex-dipole jet revealed by a linear model. *J. Atmos. Sci.,* **67,** 1438–1455.

Warner, C. D., and M. E. McIntyre, 2001: An ultrasimple spectral parameterization for nonorographic gravity waves. *J. Atmos. Sci.,* **58,** 1837–1857.

Watanabe, S., Y. Kawatani, Y. Tomikawa, K. Miyazaki, M. Takahashi, and K. Sato, 2008: General aspects of a T213L256 middle atmosphere general circulation model. *J. Geophys. Res.,* **113,** D12110, doi:10.1029/2008JD010026.